Journal of Alloys and Compounds 1042 (2025) 183927

Contents lists available at ScienceDirect

Journal of Alloys and Compounds

journal homepage: www.elsevier.com/locate/jalcom

Effect of Ni and Fe content on the plastic deformation behavior of Co–Cr–Fe–Ni–Mo alloys: A combined computational and experimental study

Kai Hiyama [a,*], Tomoki Nakajima [a], Ryoji Sahara [b], Kyosuke Ueda [a], Takayuki Narushima [a]

[a] Department of Materials Processing, Graduate School of Engineering, Tohoku University, 6-6-02, Sendai 980-8579, Japan
[b] Research Center for Structural Materials, National Institute for Materials Science, 1-2-1 Sengen, 305-0047, Japan

ARTICLE INFO

Keywords:
Co–Cr alloy
High entropy alloy
Biomedical
Stacking fault energy
First-principles calculation
Special quasi-random structure
Mechanical properties

ABSTRACT

ASTM F1058 Co–22Cr–17Fe–15Ni–4Mo (mol%) alloys (equivalent to Co–20Cr–16Fe–15Ni–7Mo in mass%) are widely used in biomedical applications, particularly in balloon-expandable stents, which require a combination of high ultimate tensile strength (UTS), good ductility, and low 0.2 % proof strength. To optimize the mechanical properties of these alloys, it is essential to understand their plastic deformation behavior. In this study, first-principles calculations, microstructural analysis, and mechanical property evaluation were used to investigate the stacking fault energy (SFE) and plastic deformation behavior of these alloys as a function of their Ni and Fe content. First-principles calculations indicated that their SFE increased with increasing Ni and Fe content, with Ni influencing the SFE more than Fe. Experimentally, increasing the Ni content suppressed the γ-to-ε stress-induced martensitic transformation during plastic deformation, resulting in improved ductility without compromising strength. With increasing Ni content, the plastic deformation mechanism in the early stage changed from martensitic transformation and/or deformation twinning to dislocation slip, attributable to an increase in the SFE. This study indicates that SFE evaluation by first-principles calculations is an effective approach for designing Co–Cr-based multicomponent systems from the perspective of plastic deformation mechanisms.

1. Introduction

High-entropy alloys (HEAs), first proposed by Cantor et al. [1] and Yeh et al. [2], have attracted considerable attention in recent years. HEAs and other multicomponent alloys with a face-centered cubic (fcc) structure possess high compositional freedom and exhibit remarkable properties. In particular, their low stacking fault energy (SFE) promotes deformation twinning and strain-induced martensitic transformation (SIMT), enabling these alloys to overcome the strength-ductility trade-off [3–5]. Notably, Co–Cr–Fe–Ni–Mo alloys with a fcc structure (γ-phase) exhibit high ultimate tensile strength (UTS) and ductility, with Mo primarily contributing toward solid-solution strengthening [6–13]. The Co–22Cr–17Fe–15Ni–4Mo alloys (mol%) (equivalent to Co–20Cr–16Fe–15Ni–7Mo in mass%), also known as ASTM F1058, are widely used in medical applications, including balloon-expandable stents and medical wires [14–16], which require high UTS, good ductility, and a low 0.2 % proof strength owing to application in plastically deformed states [16–18]. To optimize the mechanical properties of these alloys, it is essential to understand their plastic deformation behavior. The plastic deformation behavior of Co-based alloys depends on their SFE [19]. Several studies have reported the effects of alloying elements on the SFE of Co–Cr–Fe–Ni–Mo alloys [6,9,20,21]. Similar to HEAs, ASTM F1058 alloys have been reported to achieve simultaneous improvements in strength and ductility through deformation twinning [21], indicating that precise control of SFE in ASTM F1058 alloys is a promising strategy for further enhancing their mechanical properties. To achieve this, first-principles calculations have been used to estimate the SFE, even for negative values [6,22–27]. Two primary methods are used for SFE calculations: the exact muffin-tin orbital-coherent potential approximation (EMTO-CPA) method based on the mean-field theory, and the supercell method combined with a special quasi-random structure (SQS) [28]. Wei et al. [6] calculated the generalized stacking fault energy (GSFE) of Co–Cr–Fe–Ni–Mo alloys using the EMTO-CPA method; however, this approach does not account

---

* Corresponding author.
E-mail address: hiyama.kai.p2@dc.tohoku.ac.jp (K. Hiyama).

https://doi.org/10.1016/j.jallcom.2025.183927
Received 11 July 2025; Received in revised form 1 September 2025; Accepted 20 September 2025

Table 1
Abbreviations and compositions of the (a) quaternary and quinary alloys and (b) binary and ternary alloys in the calculations along with their GSFEs, and in (c) experiments along with their grain sizes.

(a)

Group in calculations	Abbreviation	Composition (number of atoms in 108-atom-supercell)					Generalized stacking fault energy/mJ·m^{-2}			
		Co	Cr	Fe	Ni	Mo	γ_{USF}	γ_{ISF}	γ_{UTF}	γ_{ESF}
Base-cal	$Co_{0.42}Cr_{0.23}Fe_{0.16}Ni_{0.15}Mo_{0.05}$	45	25	17	16	5	287	–12	300	89
(56–*x*)Co16Fe*x*Ni	$Co_{0.31}Cr_{0.23}Fe_{0.16}Ni_{0.25}Mo_{0.05}$	34	25	17	27	5	339	79	392	87
	$Co_{0.56}Cr_{0.23}Fe_{0.16}Mo_{0.05}$	61	25	17	–	5	309	–40	250	–50
(57–*y*)Co*y*Fe15Ni	$Co_{0.31}Cr_{0.23}Fe_{0.27}Ni_{0.15}Mo_{0.05}$	33	25	29	16	5	317	14	359	82
	$Co_{0.57}Cr_{0.23}Ni_{0.15}Mo_{0.05}$	62	25	–	16	5	360	–24	361	58

(b)

Abbreviation	Composition (number of atoms in 144-atom-supercell)				Generalized stacking fault energy/mJ·m^{-2}			
	Co	Cr	Fe	Ni	γ_{USF}	γ_{ISF}	γ_{UTF}	γ_{ESF}
$Co_{0.75}Ni_{0.25}$	108	–	–	36	285	–82	244	–65
$Co_{0.64}Cr_{0.25}Ni_{0.11}$	92	36	–	16	261	–159	154	–158
$Co_{0.75}Fe_{0.25}$	108	–	36	–	237	84	295	95
$Co_{0.64}Cr_{0.25}Fe_{0.11}$	92	36	16	–	255	–140	218	–169

(c)

Group in experiments	Abbreviation	Composition (mol%)							Grain size/μm
		Co	Cr	Fe	Ni	Mo	Mn	C	*d*
Base-exp	$Co_{0.40}Cr_{0.22}Fe_{0.17}Ni_{0.15}Mo_{0.04}$	39.5	22.4	16.9	14.6	4.1	2.0	0.40	18
(55–*x*)Co16Fe*x*Ni	$Co_{0.45}Cr_{0.23}Fe_{0.16}Ni_{0.10}Mo_{0.04}$	44.6	22.6	16.4	9.9	4.1	2.0	0.43	15
	$Co_{0.49}Cr_{0.23}Fe_{0.16}Ni_{0.05}Mo_{0.04}$	49.3	22.7	16.4	5.0	4.2	2.0	0.40	16
	$Co_{0.54}Cr_{0.23}Fe_{0.16}Mo_{0.04}$	54.4	22.9	16.0	–	4.2	2.1	0.39	8
(55–*y*)Co*y*Fe15Ni	$Co_{0.45}Cr_{0.23}Fe_{0.11}Ni_{0.15}Mo_{0.04}$	44.6	22.5	10.8	15.4	4.1	2.1	0.38	15
	$Co_{0.50}Cr_{0.23}Fe_{0.06}Ni_{0.15}Mo_{0.04}$	50.1	22.8	5.6	14.6	4.1	2.2	0.41	18
	$Co_{0.55}Cr_{0.23}Ni_{0.15}Mo_{0.04}$	54.9	23.1	–	14.9	4.3	2.3	0.44	17
(70–*x* – *y*)Co*y*Fe*x*Ni	$Co_{0.40}Cr_{0.22}Fe_{0.11}Ni_{0.21}Mo_{0.04}$	39.8	22.1	10.9	20.7	4.0	2.1	0.44	26
	$Co_{0.40}Cr_{0.22}Fe_{0.06}Ni_{0.26}Mo_{0.04}$	39.9	22.1	5.7	25.7	4.1	2.1	0.43	26
	$Co_{0.35}Cr_{0.22}Fe_{0.16}Ni_{0.20}Mo_{0.04}$	35.3	22.3	16.2	19.6	4.1	2.0	0.43	22
	$Co_{0.35}Cr_{0.22}Fe_{0.11}Ni_{0.26}Mo_{0.04}$	34.8	21.9	11.1	25.7	4.0	2.0	0.44	19
	$Co_{0.30}Cr_{0.22}Fe_{0.17}Ni_{0.24}Mo_{0.04}$	30.5	22.2	16.5	24.3	4.1	2.0	0.43	19

for local lattice distortions [29,30]. Conversely, the supercell method with an SQS can simulate random local atomic environments, enabling analyses of lattice distortions and crystal stability at the electronic-state level [31,32]. To the best of our knowledge, the SFE of Co–Cr–Fe–Ni–Mo alloys estimated by first-principles calculations via the supercell method with an SQS has not been reported to date.

Ni and Fe, which are completely solid-soluble in Co, are essential elements for the design of Co–Cr alloys. When added to pure Co, both elements increase the SFE of the system [33]. Thus, alloys with a wide range of SFEs can be designed by varying the alloy composition, particularly the content of Ni and Fe. A comprehensive understanding of the relationship between the computational prediction of SFE and its experimental analysis is indispensable.

Practically, both corrosion resistance and biocompatibility must be considered when modifying the Ni and Fe content in the alloys. It has been demonstrated that Cr and Mo effectively enhance corrosion resistance [34]. In the alloy design, the Cr and Mo contents were set to the same molar fractions as in the ASTM F1058 alloy to ensure sufficient corrosion resistance. An increase in Ni content may raise concerns regarding biocompatibility. However, the alloy with a Ni content of 36 mol% (ASTM F562 alloy, Co–36Ni–23Cr–6Mo (mol%), MP35N) [35] has been practically used in medical implants for many years. Therefore, the maximum Ni content of 27 mol% employed in this study is considered to fall within a biocompatible range, particularly when Cr and Mo are also present to enhance corrosion resistance.

This study investigates the effects of the Ni and Fe content of Co–22Cr–17Fe–15Ni–4Mo (mol%) alloys on the SFE, plastic deformation, and mechanical properties of the system. The SFE was evaluated through first-principles calculations using the supercell method combined with an SQS, and the corresponding changes in microstructural evolution during plastic deformation and mechanical properties were analyzed experimentally. Unless otherwise stated, the alloy compositions are expressed in mol% in this study.

2. Materials and methods

2.1. Materials

The alloy compositions used in the calculations and experiments are summarized in Table 1(a), (b), and (c), respectively. As for the quaternary and quinary alloys in Table 1(a), the compositional equivalent to the specified alloys (as per ASTM F1058) is labeled the Base-cal ($Co_{0.42}Cr_{0.23}Fe_{0.16}Ni_{0.15}Mo_{0.05}$) alloy, the alloys with varying values of Ni content compared with that of the Base-cal alloy are labeled (56–*x*)Co16Fe*x*Ni ($x = 0$–25), and the alloys with varying values of Fe content are labeled (57–*y*)Co*y*Fe15Ni ($y = 0$–27). To investigate the effects of Ni and Fe content on the SFE, the SFE of Co–X binary and Co–Cr–X ternary subsystems (X = Ni or Fe) was calculated. The compositions of the binary and ternary alloys are listed in Table 1(b). The labeling of the experimentally fabricated alloys (Table 1(c)) can be summarized as follows: the compositional equivalent to the specified alloys (as per ASTM F1058) is labeled the Base-exp ($Co_{0.40}Cr_{0.22}Fe_{0.17}Ni_{0.15}Mo_{0.04}$) alloy, alloys with a lower Ni and Fe content than the Base-exp alloy are labeled (55–*x*)Co16Fe*x*Ni ($x = 0$–10) and (55–*y*)Co*y*Fe15Ni ($y = 0$–11), respectively, and alloys with different values of both Ni and Fe content are labeled (70–*x*–*y*)Co*y*Fe*x*Ni ($x = 20$–26, $y = 6$–17). In both computational and experimental systems, the Cr and Mo concentrations were maintained constant, as mentioned in the Introduction, to ensure adequate corrosion resistance and biocompatibility.

While the computational alloys consist of Co, Cr, Fe, Ni, and Mo, the

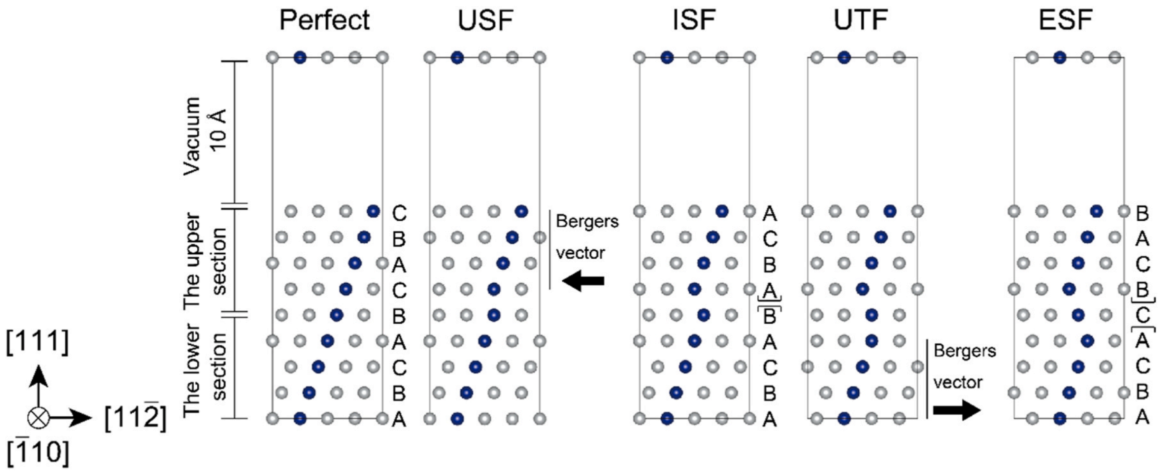

Fig. 1. Schematics of supercells with a nine-layer fcc structure and a relative translation along ⟨112⟩ direction. To clearly represent the stacking sequence and introduction of dislocation, atomic layers are color-coded: gray and blue spheres represent atoms in alternating layers.

experimental alloys include Mn and C to match the ASTM F1058 alloy composition. The exclusion of Mn and C from the computational alloys is justified as follows. Mn was excluded due to its relatively low content, as this study focused on the effects of Ni and Fe on SFE and mechanical properties in the Co–Cr–Fe–Ni–Mo system. Although C can influence SFE even at low concentrations [36,37], it is an interstitial element, and its incorporation requires systematic modeling and analysis, which is beyond the scope of this study. The effect of C on the SFE of multicomponent alloys is being investigated using first-principles calculations and will be reported in a future study.

2.2. Calculations

In multicomponent alloys, structural features such as short-range order (SRO) can significantly affect SFE and mechanical properties and therefore warrant careful consideration [27]. However, in this study, the experimental alloys underwent final heat treatment followed by quenching from high temperatures (see 2.3). From the perspective of configurational entropy, such processing is expected to promote a random atomic distribution [32]. Thus, SRO was assumed to be negligible in our calculations, and SQS models were employed to represent the random solid solution. The SQS models in this study were generated using the mcsqs code of the Alloy Theoretic Automated Toolkit [38,39], following the procedure reported by Zhou et al. [31,40]. In this approach, the random atomic distribution in alloys is described by correlation functions based on a spin representation, where an occupation variable S_i is defined at each lattice site i. As an index of SRO, the correlation function is defined as $\prod_{k,m} S_1 S_2 \cdots S_k$ for a cluster of k sites spanning a distance m. The average correlation function $\overline{\Pi}_{k,m}$ was obtained by averaging $\Pi_{k,m}$ over all symmetry-equivalent clusters in the lattice. In a perfectly random alloy, site occupation is independent of the occupation of other sites; that is, $\overline{\Pi}_{k,m} = \langle S_i \rangle^k$. Accordingly, the SQS models were optimized by minimizing the deviation, $\left(\overline{\Pi}_{k,m} - \Pi_{k,m}^{SQS}\right)^2$, ensuring that $\Pi_{k,m}^{SQS}$ closely approximates the ideal random solution for all selected k and m. In this study, k was set to 4 for $m = 2$. The resulting deviations are provided in Table S-1.

The Vienna Ab-initio Simulation Package based on density functional theory was used for GSFE calculations [41–44]. The interactions between valence electron and nuclei were modeled using projector augmented waves [45,46]. Valence electrons were treated within the generalized gradient approximation employing the Perdew–Burke–Ernzerhof formula for the exchange-correlation potential [47]. Spin-polarized calculations were conducted.

Supercells were constructed using fcc primitive cells (3 × 4 × 9 and 4 × 4 × 9). Each supercell consisted of nine layers with a total of 108 (for quaternary and quinary alloys) or 144 atoms (for binary and ternary alloys), stacked along the [111] direction. Convergence tests established the cutoff energy at 500 eV and the ***k***-point mesh at 4 × 4 × 2 for 3 × 4 × 9 supercells and 4 × 4 × 1 for 4 × 4 × 9 supercells. The convergence criterion for structural relaxation was set to 10^{-5} eV·atom^{-1}.

After structural optimization, dislocations were introduced by selecting the 4th to 6th layers from the bottom, whose compositions approximately match the overall alloy composition. Subsequently, a vacuum layer of ~10 Å was introduced along the [111] direction to eliminate interatomic interactions under three-dimensional periodic boundary conditions, followed by the introduction of dislocations. To avoid the relaxation of unstable stacking structures, such as unstable stacking fault (USF) and unstable twin fault (UTF), atomic displacements along the [111] direction were allowed during structural optimization in the GSFE calculations.

Schematics of the supercells before and after the introduction of a dislocation, viewed along the [$\bar{1}$10] direction, are shown in Fig. 1. The magnitude of the Burgers vector (b_P) was set to $\frac{a}{\sqrt{6}}$, where a represents the lattice constant after structural relaxation. In the first step, the upper section, consisting of four upper layers, was sheared using 0.5b_P and 1.0b_P (with increments of $\frac{1}{6}b_P$) along the [$\bar{1}\bar{1}$2] direction to introduce a USF and an intrinsic stacking fault (ISF), respectively. In the second step, the lower section of the ISF-introduced supercell, consisting of four lower layers, was sheared using 0.5b_P and 1.0b_P (with increments of $\frac{1}{6}b_P$) along the [11$\bar{2}$] direction to introduce a UTF and an extrinsic stacking fault (ESF), respectively. When labeling the layers A, B, and C from bottom to top along with [111] direction, the stacking sequence in a perfect crystal is ABCABCABC. For supercells containing ISFs and ESFs, the stacking sequences become ABCAB][ABCA and ABCA]C[BCAB, respectively, where the symbol '][' denotes the location of the interruption in the stacking sequence, as shown in Fig. 1. The GSFE (γ_{GSF}), considering USFs, ISFs, UTFs, and ESFs, was calculated using the following equation:

$$\gamma_{GSF} = \frac{E_{GSF} - E_0}{A} \tag{1}$$

where E_{GSF} is the total energy of the system with the GSF, E_0 is the total energy of a relaxed perfect crystal, and A is the area of the stacking-fault plane. Notably, the value of γ_{ISF} corresponds to the SFE at 0 K.

The accuracy of the calculations was validated by determining the ISF energy (γ_{ISF}) of pure Ni. The nearly equal calculated values of γ_{ISF} for the 3 × 4 × 9 and 4 × 4 × 9 supercells (128 and 135 mJ·m^{-2},

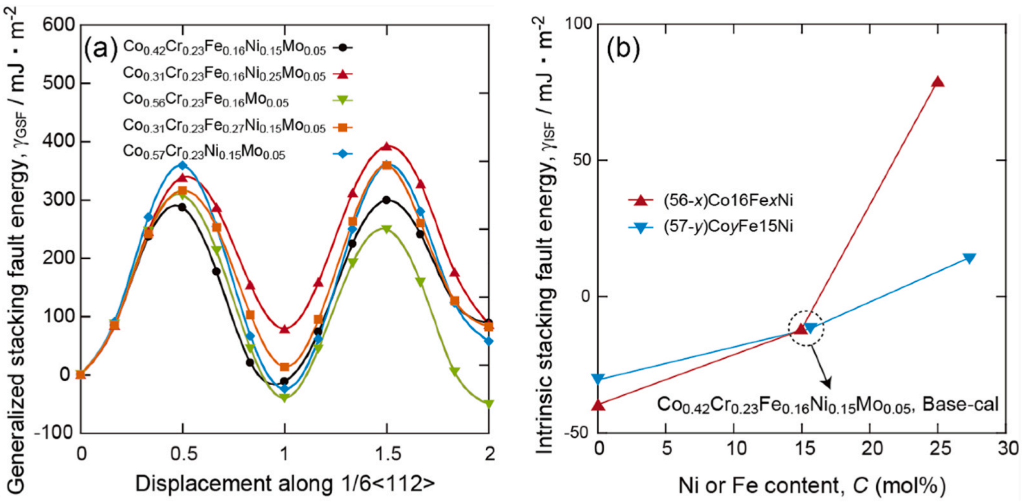

Fig. 2. (a) Generalized stacking fault energy curves and (b) changes in γ_{ISF} with the Ni or Fe content.

respectively) are consistent with the literature ($\gamma_{ISF} = 121–137$ mJ·m^{-2}) [24,48,49], confirming the accuracy of the calculations reported in this study.

2.3. Experimental

Alloy ingots (ϕ20 mm, 500 g) with the compositions listed in Table 1 (c) were fabricated by high-frequency induction melting under Ar using pure metals and Cr_3C_2 powder as raw materials. Because the carbon content of ASTM F1058 lies within 0.24–0.72 mol% (0.05–0.15 mass%), ∼0.4 mol% of carbon was added to the alloys used in experiments. The ingots were hot-forged in air at 1473 K to reduce their diameter to ϕ12 mm and then machined to ϕ10 mm. The heat-treatment procedures used in this study are reported in detail elsewhere [21]. Briefly, the specimens were subjected to solution-treatment in SiO_2 ampoules with Ar gas at a pressure of approximately 0.03 MPa at room temperature at 1473 K for 18 ks. Cold swaging in air caused a diameter reduction to ϕ7.0 mm in most specimens, except for (55–*x*)Co15Fe*x*Ni ($x = 0–10$) alloys, in which the diameter was reduced to ϕ8.0 mm. The swaged alloy bars were heat-treated in SiO_2 ampoules with Ar gas at a pressure of approximately 0.03 MPa at room temperature at 1273–1323 K for 0.9 ks followed by water quenching. Subsequently, scanning electron microscopy–electron backscatter diffraction (SEM–EBSD, JSM-7800F, JSM-IT800, JEOL Ltd. Tokyo, Japan) and transmission electron microscopy (TEM, JEM-2100, JEOL Ltd. Tokyo, Japan) were used for microstructural analysis. The mechanical properties of the alloys were evaluated using a tensile testing machine (RTF-1325, A&D Co., Ltd. Tokyo, Japan). The tensile tests were performed in accordance with the ASTM E8 [50]. Alloy bars were processed into specimens with a gauge length of 10 mm and a diameter of ϕ3 mm and tested at room temperature under a nominal strain rate of 1.67×10^{-4} s^{-1} .

3. Results and discussion

3.1. Effect of Ni and Fe content on SFE

The calculated GSFE curves for the Co–Cr–Fe–Ni–Mo alloys are shown in Fig. 2(a). Table 1(a) summarizes the calculated USF, ISF, UTF, and ESF energies (γ_{USF}, γ_{ISF}, γ_{UTF}, and γ_{ESF}, respectively). For all systems, the GSFE shows local maxima at sheared increments of $0.5b_P$ (γ_{USF}) and $1.5b_P$ (γ_{UTF}) with a local minimum at $1.0b_P$ (γ_{ISF}), resulting in bimodal curves.

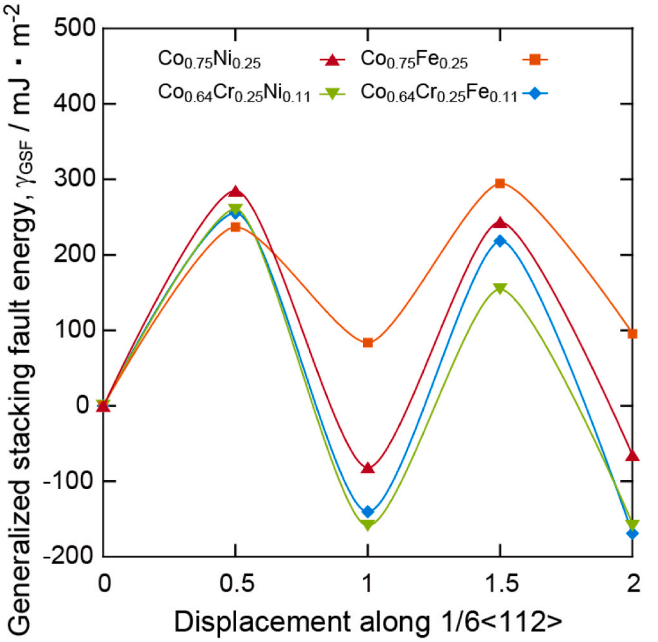

Fig. 3. Generalized stacking fault energy curves of $Co_{0.75}Fe_{0.25}$, $Co_{0.64}Cr_{0.25}Fe_{0.11}$, $Co_{0.75}Ni_{0.25}$, and $Co_{0.64}Cr_{0.25}Ni_{0.11}$ alloys.

The changes in γ_{ISF} with the addition of Ni or Fe are shown in Fig. 2 (b). Replacing Co with Ni or Fe increases the γ_{ISF}; replacement with Ni causes a more significant increase in γ_{ISF} than that with Fe. This trend differs from the first-principles calculation results for Co–X binary systems reported by Achmad et al. [51–53], which indicate that replacement with Fe increases the γ_{ISF} more significantly than that with Ni. Achmad et al. use fcc supercells composed of 20 or 22 atoms with alloying elements segregated around the ISF. An experimental study by Morral [54] indicates that Fe increases the SFE more than Ni in Co–X binary systems. In contrast, a study by Ikeda et al. [25] investigating the effects of alloy composition around stacking faults on γ_{ISF} using first-principles calculations with the EMTO-CPA method indicates that the γ_{ISF} of Co–Cr–Fe–Mn–Ni alloys increases with increasing atomic fraction of Ni or Fe near the stacking fault, with the increase being more significant for Ni than for Fe. Thus, according to Ikeda et al., the γ_{ISF} in Co–Cr–Fe–Mn–Ni alloys increases more on Ni addition than on Fe addition. The trend of the calculation results obtained in this study, which indicates that the γ_{ISF} increases more on Ni addition than on Fe addition, aligns with the trend reported by Ikeda et al. Notably, multicomponent alloys containing Cr are used in both studies. The interaction

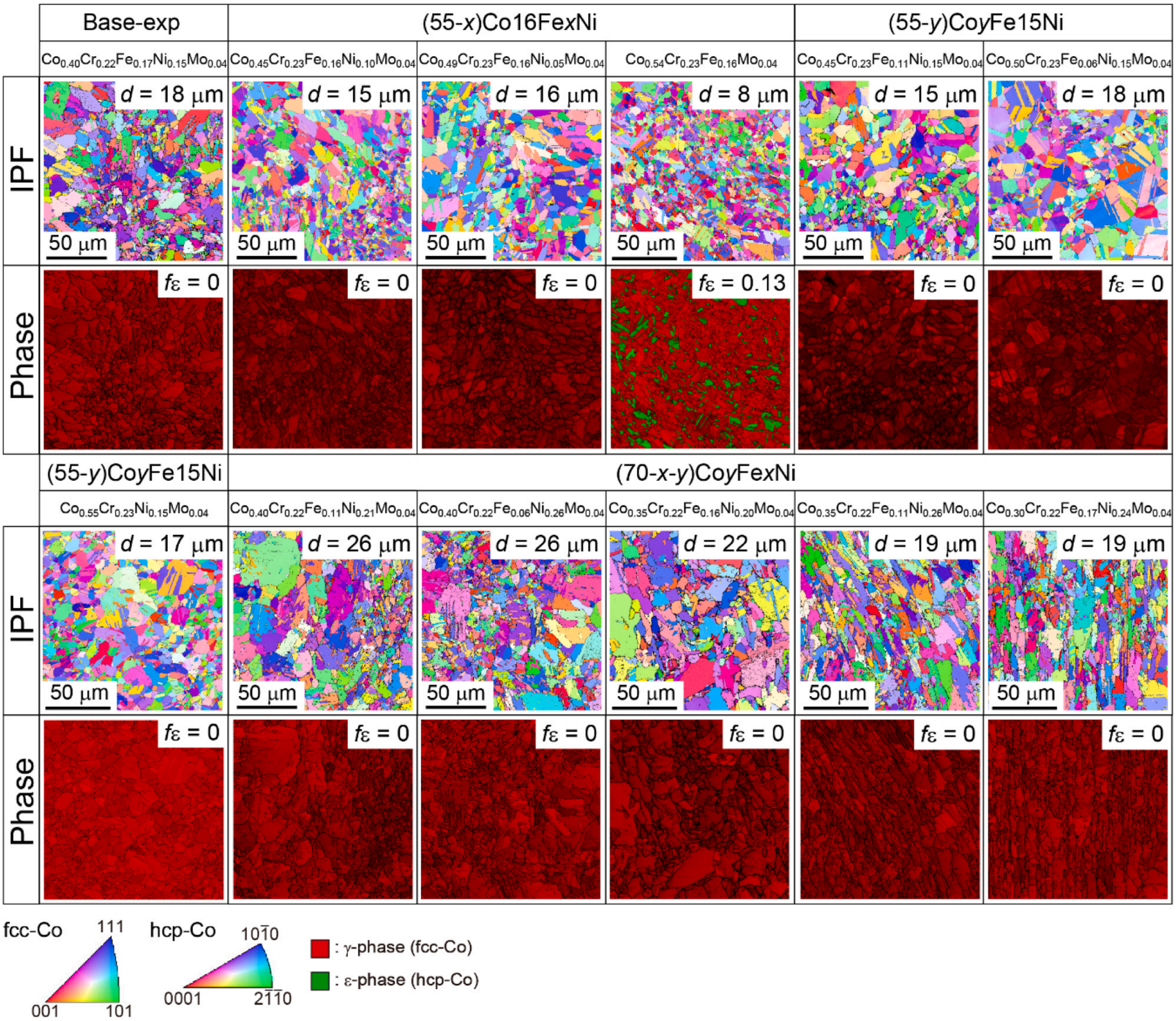

Fig. 4. EBSD inverse pole figure (IPF) and phase maps of the alloys after heat treatment at 1273 K for 0.9 ks.

between Cr and Ni or Fe in Co–Cr multicomponent alloys is considered to be associated with the γ_{ISF} of such systems. To examine the effects of Ni and Fe on the SFE further, GSFE calculations were conducted for Co–X binary and Co–Cr–X ternary systems (X = Ni or Fe). The GSFE curves of $Co_{0.75}Fe_{0.25}$, $Co_{0.64}Cr_{0.25}Fe_{0.11}$, $Co_{0.75}Ni_{0.25}$, and $Co_{0.64}Cr_{0.25}Ni_{0.11}$ are shown in Fig. 3, while Table 1(b) lists their compositions and γ_{USF}, γ_{ISF}, γ_{UTF}, and γ_{ESF} values. Binary systems containing Fe show a larger value of γ_{ISF} than those containing Ni, consistent with

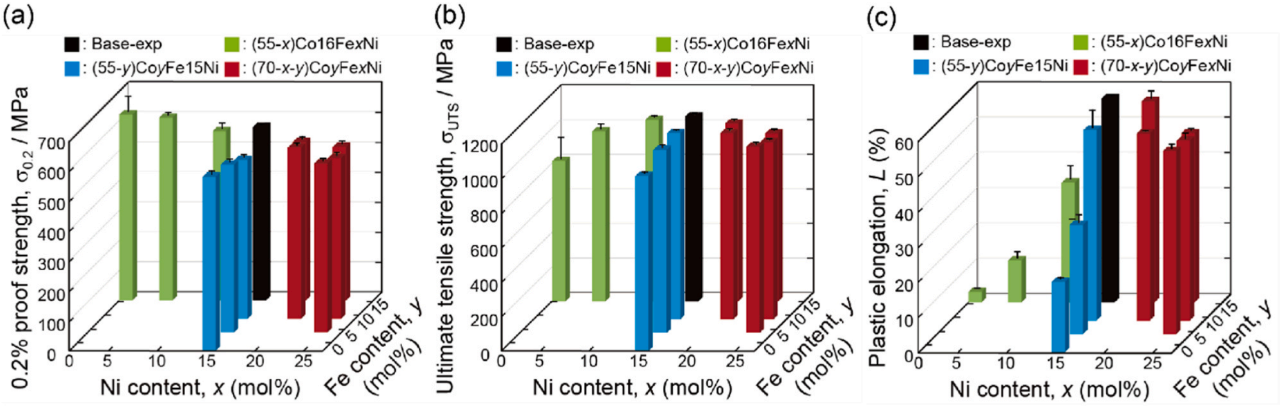

Fig. 5. Mechanical property changes in alloys heat-treated at 1273 K for 0.9 ks with varying values of Ni or Fe content: (a) 0.2 % proof strength, (b) ultimate tensile strength, and (c) plastic elongation.

Table 2
Summary of mechanical properties and the ε-phase fraction after alloy fracture.

Group in experiments	Abbreviation	0.2 % proof strength (MPa)	Ultimate tensile strength (MPa)	Plastic elongation (%)	ε-phase fraction after fracture (%)
Base-exp	$Co_{0.40}Cr_{0.22}Fe_{0.17}Ni_{0.15}Mo_{0.04}$	578 ± 6	1069 ± 12	53 ± 1	5
(55–*x*)Co 16Fe*x*Ni	$Co_{0.45}Cr_{0.23}Fe_{0.16}Ni_{0.10}Mo_{0.04}$	565 ± 22	1050 ± 13	34 ± 4	27
	$Co_{0.49}Cr_{0.23}Fe_{0.16}Ni_{0.05}Mo_{0.04}$	610 ± 13	983 ± 36	12 ± 2	32
	$Co_{0.54}Cr_{0.23}Fe_{0.16}Mo_{0.04}$	620 ± 55	812 ± 126	3 ± 1	31
(55–*y*)Co *y*Fe15Ni	$Co_{0.45}Cr_{0.23}Fe_{0.11}Ni_{0.15}Mo_{0.04}$	530 ± 12	1078 ± 7	54 ± 5	10
	$Co_{0.50}Cr_{0.23}Fe_{0.06}Ni_{0.15}Mo_{0.04}$	560 ± 14	1059 ± 23	31 ± 3	5
	$Co_{0.55}Cr_{0.23}Ni_{0.15}Mo_{0.04}$	580 ± 15	1013 ± 15	20 ± 1	2
(70–*x*–*y*)Co *y*Fe*x*Ni	$Co_{0.40}Cr_{0.22}Fe_{0.11}Ni_{0.21}Mo_{0.04}$	571 ± 11	1077 ± 17	53 ± 1	0
	$Co_{0.40}Cr_{0.22}Fe_{0.06}Ni_{0.26}Mo_{0.04}$	564 ± 13	1078 ± 19	52 ± 2	0
	$Co_{0.35}Cr_{0.22}Fe_{0.16}Ni_{0.20}Mo_{0.04}$	529 ± 11	1029 ± 16	57 ± 3	0
	$Co_{0.35}Cr_{0.22}Fe_{0.11}Ni_{0.26}Mo_{0.04}$	536 ± 14	1027 ± 13	51 ± 2	0
	$Co_{0.30}Cr_{0.22}Fe_{0.17}Ni_{0.24}Mo_{0.04}$	513 ± 14	972 ± 16	48 ± 1	0

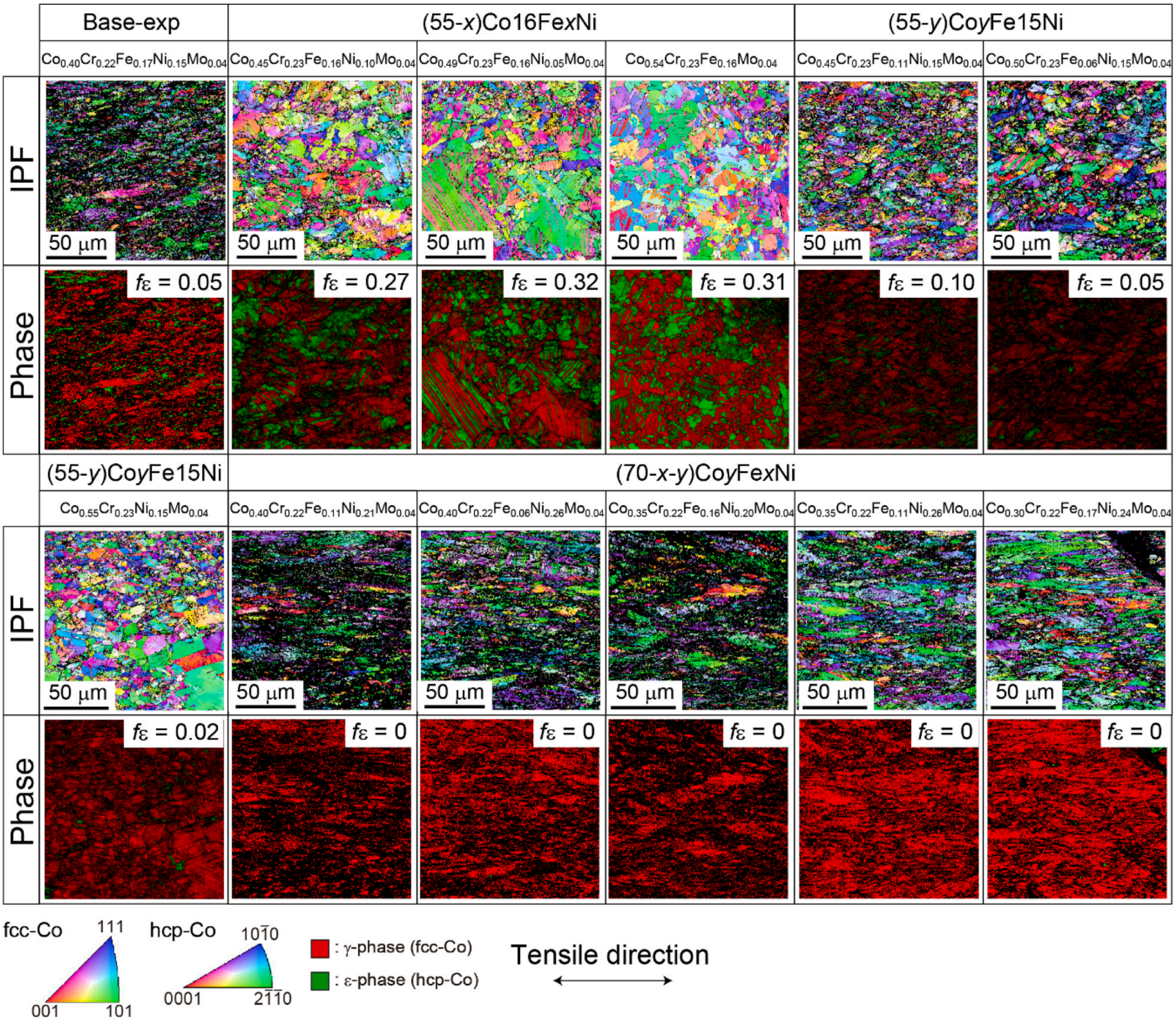

Fig. 6. EBSD IPF and phase maps of the alloys near the fracture surface.

the results of Achmad et al. In contrast, ternary systems containing Cr show comparable γ_{ISF} values, regardless of the presence of Ni or Fe. These results suggest that Fe increases the SFE in Co–X binary systems significantly; this SFE enhancement ability of Fe is adversely affected by the presence of Cr in the system. Moreover, the effects of Ni and Fe on the SFE are different for Co-based binary alloys and Cr-containing Co–Cr multicomponent alloys. Similar to Cr, Mo is one of the principal alloying elements in Co–Cr alloys and is expected to interact with Ni and Fe, potentially influencing the SFE. We are currently conducting both computational and experimental studies to investigate the effect of Mo content on the SFE of Co–Cr alloys.

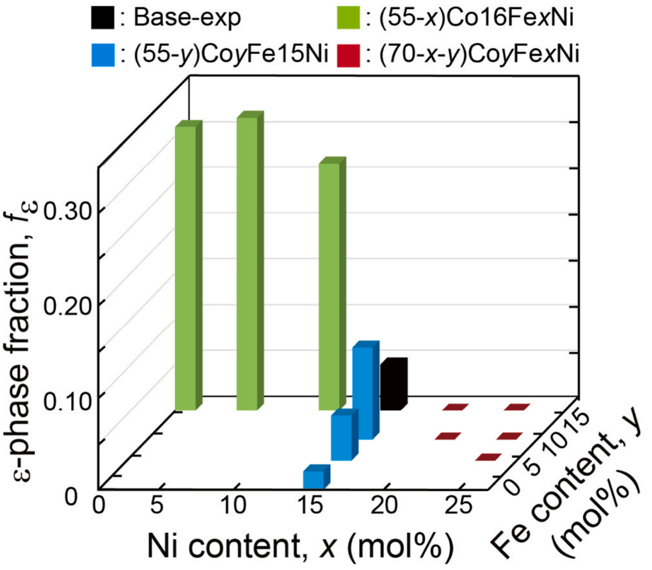

Fig. 7. (a) ε-phase fractions in the vicinity of the fracture surface of the alloys and TEM bright-field images of the (b) Base-exp and (c) $\mathrm{Co_{0.49}Cr_{0.23}Fe_{0.16}Ni_{0.05}Mo_{0.04}}$ alloys, both heat-treated at 1323 K for 0.9 ks and subjected to 5 % true strain.

3.2. Microstructure and mechanical properties

The EBSD images and grain sizes (*d*) of all the alloys subjected to mechanical-property analyses are presented in Fig. 4 and Table 1(c), respectively. The 0.2 % proof strength, UTS, and plastic elongation as functions of Ni or Fe content are shown in Fig. 5(a)–(c), respectively, and the mechanical properties are summarized in Table 2. For most alloys, the 0.2 % proof strength and UTS values vary within 500–600 MPa and 1000–1080 MPa, respectively. Moreover, an increase in Ni or Fe content leads to an increase in plastic elongation (Fig. 5(c)). Representative true stress–true strain curves and work hardening rates are shown in Fig. S-1. For $\mathrm{Co_{0.30}Cr_{0.22}Fe_{0.17}Ni_{0.24}Mo_{0.04}}$ alloy, which has a significantly higher Ni content, the work hardening rate remains low throughout the entire plastic deformation process compared with the Base-exp ($\mathrm{Co_{0.40}Cr_{0.22}Fe_{0.17}Ni_{0.15}Mo_{0.04}}$) alloy.

The EBSD images of the alloys near the fracture surfaces, which are used to measure the ε-phase (hexagonal closed-pack) fraction of the alloys, are shown in Fig. 6. The ε-phase fraction of the alloys as a function of their Ni and Fe content is shown in Fig. 7. The ε-phase is formed by γ-to-ε strain-induced martensitic transformation (SIMT) during plastic deformation. The ε-phase fraction decreases significantly with increasing Ni content, indicating a significant contribution of dislocation slip toward the plastic deformation mechanism. Representative XRD patterns of tensile-tested specimens are shown in Fig. S-2. The experimental details on the XRD measurements are provided in the Supplemental Materials. All specimens consisted of a single γ-phase before the tensile test. After testing, the $\mathrm{Co_{0.49}Cr_{0.23}Fe_{0.16}Ni_{0.05}Mo_{0.04}}$ alloy exhibited a significant amount of ε-phase, while the $\mathrm{Co_{0.55}Cr_{0.23}Ni_{0.15}Mo_{0.04}}$ alloy showed a small amount of ε-phase. In contrast, the $\mathrm{Co_{0.35}Cr_{0.22}Fe_{0.16}Ni_{0.20}Mo_{0.04}}$ alloy remained a single γ-phase with no ε-phase formation. These results indicate that both Ni and Fe suppress ε-phase formation via SIMT, with Ni having a more pronounced effect. These observations are consistent with the EBSD results near the fracture surface shown in Fig. 6. TEM bright-field images of the Base-exp and $\mathrm{Co_{0.49}Cr_{0.23}Fe_{0.16}Ni_{0.05}Mo_{0.04}}$ alloys, respectively, after heat treatment followed by the introduction of 5 % true strain, are shown in Fig. 8. The Ni content of the Base-exp alloy (15 mol%) is higher than that of the $\mathrm{Co_{0.49}Cr_{0.23}Fe_{0.16}Ni_{0.05}Mo_{0.04}}$ alloy (5 mol%). Notably, planar dislocations and stacking faults are predominantly observed in the Base-exp and $\mathrm{Co_{0.49}Cr_{0.23}Fe_{0.16}Ni_{0.05}Mo_{0.04}}$ alloys, respectively, indicating that the primary deformation mechanism in the early stage is dislocation slip in the former and martensitic transformation and/or deformation twinning in the latter. With increasing Ni content, the plastic deformation mechanism changes from martensitic transformation and/or twinning to dislocation slip, reflecting a corresponding increase in SFE, in agreement with first-principles calculations.

3.3. Relationship between SFE and mechanical properties for alloy designing

The effects of Ni and Fe on the γ_{ISF} (SFE) estimated using calculations and experimentally determined mechanical properties, such as plastic elongation, UTS, and 0.2 % proof strength, are shown in Fig. 9. Both γ_{ISF} and plastic elongation increase with increasing addition of Ni and Fe (Fig. 9(a) and (b)). In Co–Cr alloys, the interface between the γ- and ε-phases functions as a crack-initiation site [21,55,56]. Therefore, reducing the ε-phase fraction likely improves ductility. The formation of the ε-phase by SIMT is suppressed by an increase in SFE. Thus, increasing the SFE by adding Ni and Fe is an effective method for enhancing the ductility of the system. Notably, the increase in plastic deformation with increasing Ni and Fe addition saturates at ~15 and 10 mol%, respectively, indicating a limit to the SFE-increment effect on the ductility of Co–Cr alloys.

The changes in strength with increasing Ni and Fe content are minimal (Fig. 9(c) and (d)). In Co–Cr–Fe–Ni–Mo alloys, controlling the SFE and plastic deformation mechanism by adjusting the Ni and Fe content, particularly the Ni content, which significantly contributes toward increasing the SFE, enables alloy design that improves ductility while maintaining a high UTS and low 0.2 % proof strength. Besides contributing toward the design of biomedical Co–Cr alloys, the insights obtained in this study are expected to drive further development of high- and medium-entropy alloys.

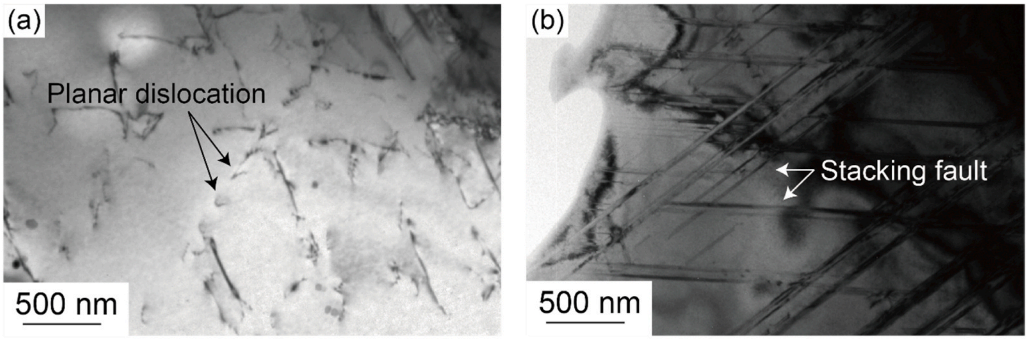

Fig. 8. TEM bright-field images of the (a) Base-exp and (b) $\mathrm{Co_{0.49}Cr_{0.23}Fe_{0.16}Ni_{0.05}Mo_{0.04}}$ alloys, both heat-treated at 1323 K for 0.9 ks and subjected to 5 % true strain.

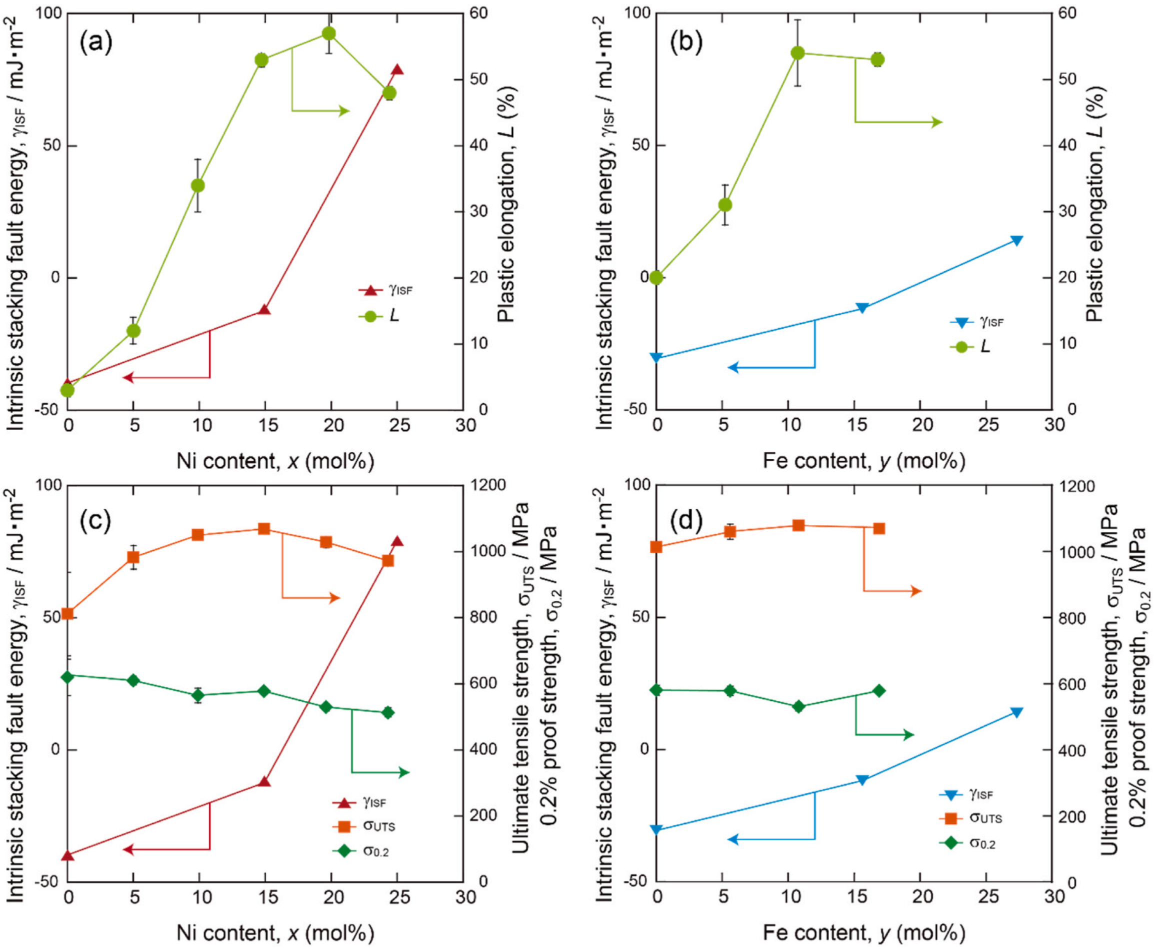

Fig. 9. Changes in γ_{ISF} and mechanical properties with (a, c) Ni or (b, d) Fe content. (a, b) and (c, d) show the variations in plastic elongation and strength, respectively.

4. Conclusions

This study investigated the effects of Ni and Fe content on the plastic deformation behavior of Co–Cr–Fe–Ni–Mo alloys through a combination of computational and experimental approaches. The findings of this study can be summarized as follows:

- The γ_{ISF} (SFE) derived from first-principles calculations increases with increasing addition of Ni and Fe; this increase is more pronounced with Ni addition than with Fe addition.
- The formation of the ε-phase, associated with the γ-to-ε SIMT observed in fractured alloys, decreases with increasing Ni content. This implies that an increase in Ni content increases the SFE, consistent with the computational results of this study.
- With increasing Ni content, the plastic deformation mechanism in the early stage changes from martensitic transformation and/or deformation twinning to dislocation slip.
- As the Ni and Fe content increases, the strength of the alloy remains unchanged, whereas its plastic elongation increases through the suppression of SIMT.
- These findings demonstrate that first-principles calculations can accurately evaluate the SFE, which can be used to understand the plastic deformation behavior in Co–Cr-based multicomponent systems.

Thus, this study contributes significantly toward alloy research and is expected to guide future studies on the design and development of high-performance multicomponent alloys with unique characteristics for biomedical and other specialized applications.

CRediT authorship contribution statement

Kai Hiyama: Writing – original draft, Writing – review & editing, Investigation, Methodology, Formal analysis, Visualization, Conceptualization. **Tomoki Nakajima:** Writing – review & editing, Investigation, Methodology. **Ryoji Sahara:** Writing – review & editing, Methodology, Funding Acquisition, Resources. **Kyosuke Ueda:** Writing – review & editing, Data curation. **Takayuki Narushima:** Writing – review & editing, Supervision, Project administration.

Funding

This study was partially supported by NIMS Joint Research Hub Program (Grant No. 2025-014) and the Japan Society for the Promotion of Science (JSPS) KAKENHI grant (Grant No. 24K01149).

Declaration of Competing Interest

The authors declare that no commercial interests or relationships have influenced this paper.

Acknowledgements

We thank Dr. K. Kobayashi of Tohoku University for TEM analysis. Calculations were performed using the Numerical Materials Simulator at NIMS and the supercomputing system at the Institute for Materials

Research (IMR), Tohoku University (Proposal Nos. 202212-SCKXX-0506 and 202312-SCKXX-0502).

Appendix A. Supporting information

Supplementary data associated with this article can be found in the online version at doi:10.1016/j.jallcom.2025.183927.

Data availability

Data supporting the findings of this study are available from the corresponding author upon reasonable request.

References

[1] B. Cantor, I.T.H. Chang, P. Knight, A.J.B. Vincent, Microstructural development in equiatomic multicomponent alloys, 377, Mater. Sci. Eng. A 375 (2004) 213–218, https://doi.org/10.1016/j.msea.2003.10.257.

[2] J.-W. Yeh, S.-K. Chen, S.-J. Lin, J.-Y. Gan, T.-S. Chin, T.-T. Shun, C.-H. Tsau, S.-Y. Chang, Nanostructured high-entropy alloys with multiple principal elements: novel alloy design concepts and outcomes, Adv. Eng. Mater. 6 (2004) 299–303, https://doi.org/10.1002/adem.200300567.

[3] Y. Deng, C.C. Tasan, K.G. Pradeep, H. Springer, A. Kostka, D. Raabe, Design of a twinning-induced plasticity high entropy alloy, Acta Mater. 94 (2015) 124–133, https://doi.org/10.1016/j.actamat.2015.04.014.

[4] Z. Li, K.G. Pradeep, Y. Deng, D. Raabe, C.C. Tasan, Metastable high-entropy dual-phase alloys overcome the strength–ductility trade-off, Nature 534 (2016) 227–230, https://doi.org/10.1038/nature17981.

[5] T.L. Achmad, S.T. Prasetya Aji, A.A. Korda, Development of CoCrWNi alloy through stacking fault energy modeling by first-principles, computational thermodynamic, and experimental methods, Met. Mater. Int. (2025), https://doi.org/10.1007/s12540-025-01894-y.

[6] D. Wei, X. Li, S. Schönecker, J. Jiang, W.-M. Choi, B.-J. Lee, H.S. Kim, A. Chiba, H. Kato, Development of strong and ductile metastable face-centered cubic single-phase high-entropy alloys, Acta Mater. 181 (2019) 318–330, https://doi.org/10.1016/j.actamat.2019.09.050.

[7] J. Li, K. Yamanaka, A. Chiba, Significant lattice-distortion effect on compressive deformation in Mo-added CoCrFeNi-based high-entropy alloys, Mater. Sci. Eng. A 830 (2022) 142295, https://doi.org/10.1016/j.msea.2021.142295.

[8] J. Li, K. Yamanaka, A. Chiba, Calculation-driven design of off-equiatomic high-entropy alloys with enhanced solid-solution strengthening, Mater. Sci. Eng. A 817 (2021) 141359, https://doi.org/10.1016/j.msea.2021.141359.

[9] J. Li, K. Yamanaka, Y. Hayasaka, A. Chiba, Suzuki hardening and segregation in $Co_{0.95}Cr_{0.8}Fe_{0.25}Ni_{1.8}Mo_{0.475}$ high-entropy alloys, Scr. Mater. 226 (2023) 115260, https://doi.org/10.1016/j.scriptamat.2022.115260.

[10] Y. Jia, Z. Wang, F. He, Q. Wu, B. Gan, J. Li, J. Wang, Revisiting MP35N and MP159: the route to ultra-strong Co–Cr–Ni medium entropy alloys, Intermetallics 143 (2022) 107507, https://doi.org/10.1016/j.intermet.2022.107507.

[11] K. Ming, X. Bi, J. Wang, Strength and ductility of CrFeCoNiMo alloy with hierarchical microstructures, Int. J. Plast. 113 (2019) 255–268, https://doi.org/10.1016/j.ijplas.2018.10.005.

[12] W. Li, X. Long, S. Huang, Q. Fang, C. Jiang, Elevated fatigue crack growth resistance of Mo alloyed CoCrFeNi high entropy alloys, Eng. Fract. Mech. 218 (2019) 106579, https://doi.org/10.1016/j.engfracmech.2019.106579.

[13] Y. Lv, Y. Guo, J. Zhang, Y. Lei, P. Song, J. Chen, Improving mechanical properties of Co-Cr-Fe-Ni high entropy alloy via C and Mo microalloying, Materials 17 (2024) 529, https://doi.org/10.3390/ma17020529.

[14] ASTM F1058-16, Standard specification for wrought 40Cobalt-20Chromium-16Iron-15Nickel-7Molybdenum alloy wire and strip for surgical implant applications (UNS R30008, 13, ASTM International, USA, 2019, p. 01, https://doi.org/10.1520/F1058-16.

[15] C.O. Clerc, M.R. Jedwab, D.W. Mayer, P.J. Thompson, J.S. Stinson, Assessment of wrought ASTM F1058 cobalt alloy properties for permanent surgical implants, J. Biomed. Mater. Res. 38 (1997) 229–234, https://doi.org/10.1002/(SICI)1097-4636(199723)38:3%3C229::AID-JBM7%3E3.0.CO;2-R.

P. Poncin, C. Millet, J. Chevy, J.L. Proft, Comparing and optimizing Co-Cr tubing for stent applications, Proc. Mater. Process. Med. Devices Conf. (2004) 279–283.

P. Poncin, J. Proft, Stent tubing: understanding the desired attributes, Proc. Mater. Process. Med. Devices Conf. (2003) 253–259.

[18] A. Khalilimeybodi, A.A. Khoei, B. Sharif-Kashani, Future balloon-expandable stents: high or low-strength materials? Cardiovasc. Eng. Technol. 11 (2020) 188–204, https://doi.org/10.1007/s13239-019-00450-1.

[19] L. Rémy, A. Pineau, Twinning and strain-induced f.c.c. → h.c.p. transformation on the mechanical properties of Co-Ni-Cr-Mo alloys, Mater. Sci. Eng. 26 (1976) 123–132, https://doi.org/10.1016/0025-5416(76)90234-2.

[20] W.H. Liu, Z.P. Lu, J.Y. He, J.H. Luan, Z.J. Wang, B. Liu, Y. Liu, M.W. Chen, C.T. Liu, Ductile CoCrFeNiMox high entropy alloys strengthened by hard intermetallic phases, Acta Mater. 116 (2016) 332–342, https://doi.org/10.1016/j.actamat.2016.06.063.

[21] K. Hiyama, K. Ueki, K. Ueda, T. Narushima, Probing plastic deformation-related properties in static recrystallized Co–Cr–Fe–Ni–Mo alloy for biomedical applications, Mater. Sci. Eng. A 899 (2024) 146458, https://doi.org/10.1016/j.msea.2024.146458.

[22] X. Sun, S. Lu, R. Xie, X. An, W. Li, T. Zhang, C. Liang, X. Ding, Y. Wang, H. Zhang, L. Vitos, Can experiment determine the stacking fault energy of metastable alloys? Mater. Des. 199 (2021) 109396 https://doi.org/10.1016/j.matdes.2020.109396.

[23] S. Lu, X. Sun, Y. Tian, X. An, W. Li, Y. Chen, H. Zhang, L. Vitos, Theory of transformation-mediated twinning, PNAS Nexus 2 (2023) pgac282, https://doi.org/10.1093/pnasnexus/pgac282.

[24] S. Zhao, G.M. Stocks, Y. Zhang, Stacking fault energies of face-centered cubic concentrated solid solution alloys, Acta Mater. 134 (2017) 334–345, https://doi.org/10.1016/j.actamat.2017.05.001.

[25] Y. Ikeda, F. Körmann, I. Tanaka, J. Neugebauer, Impact of chemical fluctuations on stacking fault energies of CrCoNi and CrMnFeCoNi high entropy alloys from first principles, Entropy 20 (2018) 655, https://doi.org/10.3390/e20090655.

[26] J. Kumar, A. Linda, M. Sadhasivam, K.G. Pradeep, N.P. Gurao, K. Biswas, The effect of Si addition on the structure and mechanical properties of equiatomic CoCrFeMnNi high entropy alloy by experiment and simulation, Materialia 27 (2023) 101707, https://doi.org/10.1016/j.mtla.2023.101707.

[27] V. Shivam, D. Beniwal, Y. Shadangi, P. Singh, O. Palasyuk, V.S. Hariharan, M. J. Kramer, G. Phanikumar, D.D. Johnson, P.K. Ray, N.K. Mukhopadhyay, Effect of Zn addition on phase evolution in AlCrFeCoNiZn high-entropy alloy, Adv. Eng. Mater. 27 (2025) 2400827, https://doi.org/10.1002/adem.202400827.

[28] A. Zunger, S.-H. Wei, L.G. Ferreira, J.E. Bernard, Special quasirandom structures, Phys. Rev. Lett. 65 (1990) 353–356, https://doi.org/10.1103/PhysRevLett.65.353.

[29] L.-Y. Tian, L.-H. Ye, Q.-M. Hu, S. Lu, J. Zhao, L. Vitos, CPA descriptions of random Cu-Au alloys in comparison with SQS approach, Comp. Mater. Sci. 128 (2017) 302–309, https://doi.org/10.1016/j.commatsci.2016.11.045.

[30] M.P.J. Punkkinen, A. Lahti, P. Laukkanen, M. Kuzmin, M. Tuominen, M. Yasir, J. Dahl, J. Mäkelä, H.L. Zhang, L. Vitos, K. Kokko, Thermodynamics of the pseudobinary $GaAs_{1-x}Bi_x$ ($0 \le x \le 1$) alloys studied by different exchange-correlation functionals, special quasi-random structures and Monte Carlo simulations, Comp. Condens. Matter 5 (2015) 7–13, https://doi.org/10.1016/j.cocom.2015.09.002.

[31] W. Zhou, R. Sahara, K. Tsuchiya, First-principles study of the phase stability and elastic properties of Ti-X alloys (X = Mo, Nb, Al, Sn, Zr, Fe, Co, and O), J. Alloy. Compd. 727 (2017) 579–595, https://doi.org/10.1016/j.jallcom.2017.08.128.

[32] H. Mizuseki, R. Sahara, K. Hongo, Order–disorder competition in equiatomic 3d–transition–metal quaternary alloys: phase stability and electronic structure, Sci. Technol. Adv. Mater. Methods 3 (2023) 2153632, https://doi.org/10.1080/27660400.2022.2153632.

C.T. Sims, N.S. Stoloff, W.C. Hagel, Superalloys II, John Wiley & Sons, New York, 1987, pp. 135–162.

[34] T. Matković, P. Matković, J. Malina, Effects of Ni and Mo on the microstructure and some other properties of Co–Cr dental alloys, J. Alloy. Compd. 366 (2004) 293–297, https://doi.org/10.1016/j.jallcom.2003.07.004.

[35] ASTM F562-22, Standard specification for wrought 35cobalt-35nickel-20chromium-10molybdenum alloy for surgical implant applications (UNS R30035), vol.13.01, ASTM International, USA, 2022. https://doi.org/10.1520/F0562-22.

[36] Y. Ikeda, I. Tanaka, J. Neugebauer, F. Körmann, Impact of interstitial C on phase stability and stacking-fault energy of the CrMnFeCoNi high-entropy alloy, Phys. Rev. Mater. 3 (2019) 113603, https://doi.org/10.1103/PhysRevMaterials.3.113603.

[37] I. Moravcik, M. Zelený, A. Dlouhy, H. Hadraba, L. Moravcikova-Gouvea, P. Papež, O. Fikar, I. Dlouhy, D. Raabe, Z. Li, Impact of interstitial elements on the stacking fault energy of an equiatomic CoCrNi medium entropy alloy: theory and experiments, Sci. Technol. Adv. Mater. 23 (2022) 376–392, https://doi.org/10.1080/14686996.2022.2080512.

[38] A. van de Walle, G. Ceder, Automating first-principles phase diagram calculations, J. Phase. Eq. 23 (2002) 348, https://doi.org/10.1361/105497102770331596.

[39] A. van de Walle, P. Tiwary, M. de Jong, D.L. Olmsted, M. Asta, A. Dick, D. Shin, Y. Wang, L.-Q. Chen, Z.-K. Liu, Efficient stochastic generation of special quasirandom structures, Calphad 42 (2013) 13–18, https://doi.org/10.1016/j.calphad.2013.06.006.

[40] W. Zhou, M. Souissi, T. Abe, R. Sahara, P.H.-L. Sit, K. Tsuchiya, Evaluating the phase stability of binary titanium alloy Ti-X (X = Mo, Nb, Al, and Zr) using first-principles calculations and a Debye model, Calphad 71 (2020) 102207, https://doi.org/10.1016/j.calphad.2020.102207.

[41] G. Kresse, J. Hafner, Ab initio molecular dynamics for liquid metals, Phys. Rev. B 47 (1993) 558–561, https://doi.org/10.1103/PhysRevB.47.558.

[42] G. Kresse, J. Hafner, Ab initio molecular-dynamics simulation of the liquid-metal-amorphous-semiconductor transition in germanium, Phys. Rev. B 49 (1994) 14251–14269, https://doi.org/10.1103/PhysRevB.49.14251.

[43] G. Kresse, J. Furthmüller, Efficiency of ab-initio total energy calculations for metals and semiconductors using a plane-wave basis set, Comp. Mater. Sci. 6 (1996) 15–50, https://doi.org/10.1016/0927-0256(96)00008-0.

[44] G. Kresse, J. Furthmüller, Efficient iterative schemes for ab initio total-energy calculations using a plane-wave basis set, Phys. Rev. B 54 (1996) 11169–11186, https://doi.org/10.1103/PhysRevB.54.11169.

[45] P.E. Blöchl, Projector augmented-wave method, Phys. Rev. B 50 (1994) 17953–17979, https://doi.org/10.1103/PhysRevB.50.17953.

[46] G. Kresse, D. Joubert, From ultrasoft pseudopotentials to the projector augmented-wave method, Phys. Rev. B 59 (1999) 1758–1775, https://doi.org/10.1103/PhysRevB.59.1758.

[47] J.P. Perdew, K. Burke, M. Ernzerhof, Generalized gradient approximation made simple, Phys. Rev. Lett. 77 (1996) 3865–3868, https://doi.org/10.1103/PhysRevLett.77.3865.

[48] A. Datta, U.V. Waghmare, U. Ramamurty, Density functional theory study on stacking faults and twinning in Ni nanofilms, Scr. Mater. 60 (2009) 124–127, https://doi.org/10.1016/j.scriptamat.2008.09.018.

[49] S.L. Shang, W.Y. Wang, Y. Wang, Y. Du, J.X. Zhang, A.D. Patel, Z.K. Liu, Temperature-dependent ideal strength and stacking fault energy of fcc Ni: a first-principles study of shear deformation, J. Phys. Condens. Matter 24 (2012) 155402, https://doi.org/10.1088/0953-8984/24/15/155402.

[50] ASTM E8/E8M-16a. Standard test methods for tension testing of metallic materials, ASTM International, USA, 2020, https://doi.org/10.1520/E0008_E0008M-16A.

[51] T.L. Achmad, W. Fu, H. Chen, C. Zhang, Z.-G. Yang, Effect of strain on the intrinsic stacking fault energy of fcc Co: a first-principles study, J. Mater. Sci. 53 (2018) 10217–10230, https://doi.org/10.1007/s10853-018-2320-6.

[52] T.L. Achmad, W. Fu, H. Chen, C. Zhang, Z.-G. Yang, Effects of alloying elements concentrations and temperatures on the stacking fault energies of Co-based alloys by computational thermodynamic approach and first-principles calculations, J. Alloy. Compd. 694 (2017) 1265–1279, https://doi.org/10.1016/j.jallcom.2016.10.113.

[53] T.L. Achmad, W. Fu, H. Chen, C. Zhang, Z.-G. Yang, First-principles calculations of generalized-stacking-fault-energy of Co-based alloys, Comp. Mater. Sci. 121 (2016) 86–96, https://doi.org/10.1016/j.commatsci.2016.04.031.

[54] F.R. Morral, Corrosion of cobalt and cobalt alloys, Corrosion 25 (1969) 307–322, https://doi.org/10.5006/0010-9312-25.7.307.

[55] S. Takeda, K. Ueki, K. Ueda, M. Nakai, T. Nakano, T. Narushima, Improvement of mechanical properties of Co–Cr–W–Ni alloy tube suitable for balloon-expandable stent applications through heat treatment, Mater. Sci. Eng. A 862 (2023) 144505, https://doi.org/10.1016/j.msea.2022.144505.

[56] S.S. Friandani, K. Hiyama, K. Ueki, K. Ueda, T. Narushima, Exceptional balance of strength and ductility in biomedical Co-Cr-W-Ni alloy with added carbon, Mater. Sci. Eng. A 908 (2024) 146722, https://doi.org/10.1016/j.msea.2024.146722.